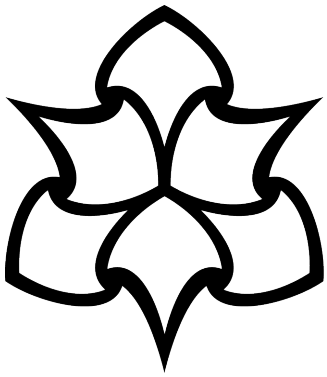

ADVANCED SUSTAINABLE SYSTEMS
www.advsustainsys.com

Recycled Additive Manufacturing Feedstocks for Fabricating High Voltage, Low-Cost Aqueous Supercapacitors

*Phatsawit Wuamprakhon, Robert D. Crapnell, Evelyn Sigley, Nicholas J. Hurst, Rhys J. Williams, Montree Sawangphruk, Edmund M. Keefe, and Craig E. Banks**

The first recycled conductive poly(lactic acid) (PLA) filament derived from post-industrial waste sources for additive manufacturing (AM) is reported herein, presenting a paradigm shift in plastic waste recycling, AM filament production, and AM energy storage architectures. Filaments utilizing a base of recycled PLA, carbon black (CB) as a conductive filler, and polyethylene glycol (PEG) as a plasticizer are used to produce aqueous AM symmetric supercapacitor platforms that can reach capacitance values 75 times higher than commercially available conductive PLA filaments. Furthermore, through the rapid prototyping capabilities of AM and GCode modification, it is seen that changing the electrode architecture from solid to a mesh with additional inter-layer spacing is able to further enhance electrode performance by 3.5 times due to improvements in the surface area, ion accommodating capabilities and faster ion diffusion. The symmetric full cell device is capable of delivering 7.82 mF cm^{-2}, 4.82 µWh cm$^{-2,}$ and 433.32 µW cm^{-2} of capacitance, energy, and power density, respectively. Moreover, the material cost is £0.15 per electrode. This work represents a new direction for plastic waste recycling, in which low-value recycled base products can be manufactured into high-value end products in their second cycles.

1. Introduction

Plastics, i.e., materials consisting of synthetic organic polymers, are extremely convenient, low-cost, lightweight, and durable materials that are utilized in many aspects of day-to-day life. However, managing the end-of-life of plastic materials has become an increasingly urgent topic due to the reliance of most virgin plastics production on non-renewable resources like oil, and the significant, harmful effects that environmentally persistent waste plastic can have on the natural world.[1] Limiting these effects requires consumption of virgin plastic to be reduced wherever possible, and where not possible, plastic waste should be recycled into new products such that it does not enter traditional waste streams (e.g., by being sent to landfill). With regards to plastics recycling, the ideal situation is one in which innovation facilitates "upcycling" of plastic waste into products that retain high value and longevity, such that the material flow from raw material to waste product is slowed significantly.[2] Seeking upcycling in this way can be especially effective when incorporated into Circular Economy (CE) practices;[2] while the precise definition of CE has not been formalized, in broad terms, it is a new economic model intended to cause a sea change in the way society approaches sustainable development.[3]

Additive Manufacturing (AM), otherwise known as 3D printing, refers to a group of technologies that manufacture objects by incremental addition of layers of material, rather than by subtraction or formation of material as in traditional techniques such as milling or molding, respectively. The AM workflow begins with design of the object using Computer-Aided Design (CAD) software, which is then digitally "sliced" into pseudo-2D layers, and finally sent to a 3D printer to be built. Production of parts in this way has a number of advantages, for example, the ability to manufacture locally and on-demand, plus it affords a high degree of part complexity and easy customization of objects. These design advantages in particular mean that polymer AM has significant potential for the upcycling of plastic waste since complex and/or bespoke parts are inherently high value.

In particular, the bespoke part production afforded by AM is becoming increasingly popular in the field of electrochemistry,[4] electrochemical equipment,[5] electroanalysis,[6] reaction mechanistic studies,[7] electrosynthesis,[8] electrocatalysis[9] and electrochemical energy storage.[10] More specifically, there has been an increasing number of publications detailing the use of

P. Wuamprakhon, R. D. Crapnell, E. Sigley, N. J. Hurst, R. J. Williams, E. M. Keefe, C. E. Banks
Faculty of Science and Engineering
Manchester Metropolitan University
Chester Street, Manchester M1 5GD, United Kingdom
E-mail: c.banks@mmu.ac.uk
P. Wuamprakhon, M. Sawangphruk
Centre of Excellence for Energy Storage Technology (CEST)
Department of Chemical and Biomolecular Engineering
School of Energy Science and Engineering
Vidyasirimedhi Institute of Science and Technology
Rayong 21210, Thailand
The ORCID identification number(s) for the author(s) of this article can be found under https://doi.org/10.1002/adsu.202200407.

DOI: 10.1002/adsu.202200407

relatively low-cost Fused Filament Fabrication (FFF) 3D printers to produce inventively designed fixtures, sample holders, and even electrodes when a conductive polymer composite material is used.[11] Producing electrochemical components by AM is not only convenient and cheap but also can afford electrode architectures not normally accessible by traditional techniques.[12] This can be especially useful in electrochemical energy storage applications.

Development of effective energy storage applications has become the subject of intense research over recent decades.[13] This is because, although sources of clean and sustainable energy such as hydroelectricity, wind, and solar are readily accessible, they are dependent on changeable environmental conditions and hence provide inconsistent power. Supercapacitors (SCs) or electrochemical capacitors (ECs) in particular have shown promise for high-power applications such as high voltage automotive, smart grids, and robotics since they can provide high specific power, long cycle life, fast charging, and high-rate capability due to their non-diffusion controlled charge storage mechanisms;[14] supercapacitors contribute to the United Nation's Sustainable Development Goals: 7: Affordable & Clean Energy, providing cutting-edge solutions to meet energy demands. Charge storage in SCs occurs either via adsorption of ions with capacitive electro-sorption at the electrode/electrolyte interface (so-called electrochemical double layer (EDL) capacitance), and/or via fast redox reactions on the electrode surface (pseudo-capacitance).[15] This allows charge–discharge at an extremely high rate. However, the energy density of such devices is relatively low compared to batteries, where the charge storage occurs via bulk faradaic reactions. Thus, the development of SCs demands a methodology for enhancing their energy density.[16] Since the amount of the stored energy (E) in SCs is directly proportional to capacitance (C) and the cell voltage (V) squared (i.e., $E = ½\ CV^2$), the ideal system for electrochemical energy storage would consist of an electrode with high capacitance and an electrolyte that is stable over a large potential window.[14c,17] Using AM can contribute in part to achieving this, specifically by allowing the production of electrodes designed to have a high surface area and hence a high area for creation of an EDL and/or redox reactions with electrolyte. However, while there have been a number of reports regarding the implementation of polymer AM toward making such capacitive energy storage devices, there are still several unresolved issues that limit performance.

One of the major obstacles in using polymer AM to produce electrochemical energy storage devices arises from the limited range of materials available for use in FFF. Specifically, conductive FFFs filaments consist of a major thermoplastic polymer component, which is non-conductive, and a minor, generally carbonaceous, conductive component. Typical materials include poly(lactic acid) (PLA) or acrylonitrile butadiene styrene (ABS) as the major, insulating component, and graphene (GP) or carbon black (CB) as the minor, conductive component. The conductive filler is usually only present in relatively small quantity, as adding too much can compromise the filament's ability to be printed. While there are commercially available conductive FFF filaments, such as Black Magic (GP/PLA) and Proto-Pasta (CB/PLA), these generally show suboptimal performance. For example, Foster et al. reported the low performance of Black Magic when printed to make stand-alone electrode in lithium-ion battery and supercapacitor.[18] Therefore, an aim of some researchers has been the development of bespoke filaments with increased concentrations of the conductive/electroactive components but which retain suitable properties for printing.[19] Some examples include the addition of active material integrated into AM feedstock to manufacture a sodium ion battery[20] and increasing the graphene content in an FFF filament used to make a current collector for metal oxide decoration in supercapacitor applications.[21]

In addition to simply improving viability for electrochemical energy storage, the manufacture of bespoke FFF filaments for such applications provides the perfect opportunity for upcycling of plastics waste; in Additively Manufactured Electrodes (AMEs), the polymer is essentially expected to act as an inert component, and since AMEs are expected to be neither load bearing nor aesthetically pleasing, deteriorations in polymer properties caused by environmental factors or thermal processing should not represent a particular concern. Furthermore, being relatively complex, electrochemical energy storage devices are likely to be of higher value than the original use of the polymer. However, as far as we are aware, there are not yet any reports of recycled polymer feedstock being used to create FFF filament for use in the manufacture of bespoke energy storage devices.

Herein, we provide the first report of Additively Manufactured SCs derived from a recycled polymer feedstock. Firstly, waste PLA recovered from coffee pods via a post-industrial waste stream was melt compounded with a plasticizer, poly(ethylene glycol) (PEG), and conductive filler, CB, with the mixture subsequently being melt extruded to make a filament suitable for FFF (**Figure 1**A). This material was then printed into a mesh-type design (Figure 1B) only achievable using AM alongside GCODE modification, which was shown to perform better as an SC than a solid electrode (Figure 1B) when analyzed as part of a half cell in a water-in-salt (WIS) electrolyte (17 M $NaClO_4$). Furthermore, meshes of bespoke material were compared to meshes printed from the commercially available conductive filament, ProtoPasta, and using the bespoke material was found to produce a better-performing SC than the commercial material, despite being obtained from recycled waste polymer. Finally, it is demonstrated how two mesh electrodes can be combined with other 3D printed components to make a fully Additively Manufactured cell for electrochemical energy storage. Overall, this work not only demonstrates how polymer AM can be used to create inventive and highly effective energy storage devices but also illustrates how waste plastics can be used strategically to address environmental issues while simultaneously creating added-value products.

2. Experimental Section

2.1. Materials and Chemical Reagents

Post-industrial waste poly(lactic acid) (PLA) was purchased from Gianeco (Turin, Italy) and was dried in an oven at 60 °C for at least 2.5 h before use. All further chemicals were used as received with no further purification. Sodium hydroxide (NaOH) (99%),

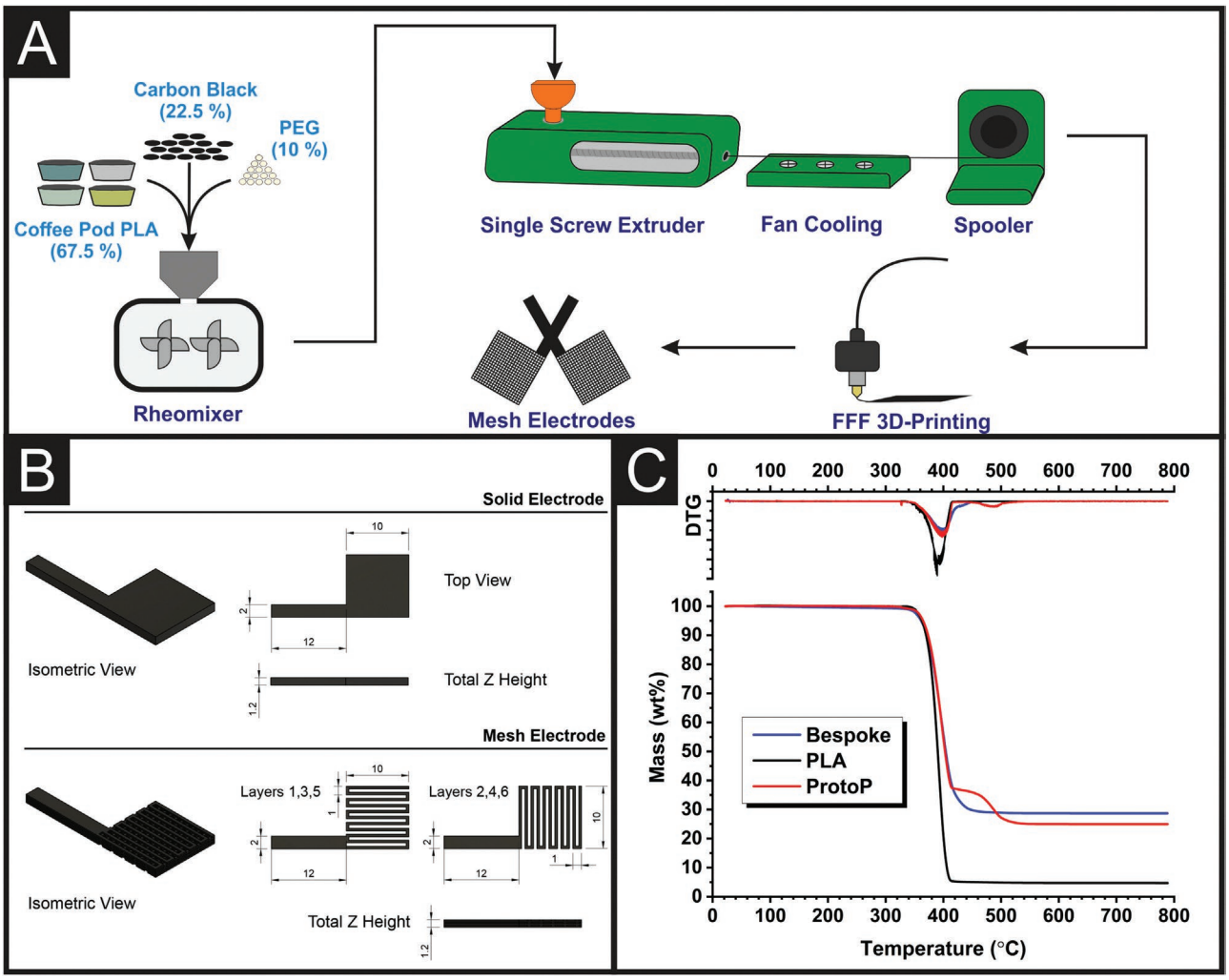

Figure 1. A) Schematic representation of the workflow, highlighting the mixing of recycled PLA, carbon black, and polyethylene glycol before filament extrusion and finally FFF printing into the desired electrodes. B) CAD images and dimensions of the additively manufactured solid and mesh electrodes used in this work. C) Thermal gravimetric analysis of the recycled PLA, commercial conductive filament, and bespoke recycled conductive filament.

polyethylene glycol (PEG, MW = 3000), and sodium perchlorate ($NaClO_4$) (98%) were purchased from Sigma Aldrich (Gillingham, UK). Carbon black (Super P, 99+%) was purchased from Fisher Scientific (Loughborough, UK). Commercial conductive CB/PLA filament (1.75 mm, Protopasta, Vancouver, Canada) was purchased from Farnell (Leeds, UK). Deionized (DI) water (18 MΩ.cm) was received from Milli-Q system (Merck, Gillingham, UK).

2.2. Preparation of Recycled Conductive Filament

Prior to mixing, the PLA pellets were dried in an oven at 60 °C for a minimum of 2.5 h to remove any residual water from the polymer. Compositions for the conductive filament were prepared based on a mixing chamber of 63 cm^3 to produce a filament with PLA (67.5%v/v), CB (22.5% v/v), and PEG (10%v/v). The chemicals were blended in a heated chamber (170 °C) with Banbury rotors at 70 rpm for 10 min using a Thermo Haake Poydrive dynameter fitted with a Thermo Haake Rheomix 600 (Thermo-Haake, Germany). The resultant sample was allowed to cool to room temperature before being granulated prior to filament extrusion using a Rapid Granulator 1528 (Rapid, Sweden). This sample was collected and added to the hopper of the EX6 extrusion line (Filabot, VA, USA), with the four heat zones set to 60, 190, 195, and 195 °C respectively. The molten polymer strand was pulled along an Airpath cooling line (Filabot, VA, USA), through an inline measure (Mitutoyo, Japan), and collected on a Filabot spooler (Filabot, VA, USA).

2.3. Additive Manufacturing

The solid electrodes used in this work were designed in Autodesk Fusion 360 (California, US) and exported as ST files. The electrodes (Figure 1B) were 10 mm x 10 mm faces with a 12 mm × 2 mm stem, all extruded to a depth of 1.2 mm. These STL files were imported into the open-source slicing software PrusaSlicer (Prusa Research, Prague, Czech Republic) where the printing parameters were defined (outlined below) and sliced to create the GCODE file ready for printing.

The Mesh electrodes, Figure 1B, were designed using FullControl G-Code Designer (FullControl).[22] Using cartesian coordinates, each layer was designed to follow an alternating path of ± 10 mm and ± 2 mm lines along the *x* and *y*-axis, connection to a stem of 12 mm in the *x*-axis and 2 mm in the *y*-axis, all to a height of 0.2 mm in the *z*-axis. This design was repeated in the *z*-axis for 6, 12, and 24 layers, and visualized in Repetier-Host, a 3D printer host and slicing software, to visualize the subsequently generated G-Code.

All AMEs were produced using FFF printing of the conductive filaments using a Prusa i3 MK3S+ 3D-printed (Prusa Research, Prague, Czech Republic). The printing parameters for all prints (using both filaments) were kept constant, using a 0.4 mm brass nozzle, 0.5 mm layer width, 0.2 mm layer height, 220 °C nozzle temperature, 65 °C bed temperature, 17 mm s^{-1} print speed and 0 fan speed.

2.4. Material Characterizations

Scanning Electron Microscopy (SEM) measurements were recorded on a Supra 40VP Field Emission (Carl Zeiss Ltd., Cambridge, UK) with an average chamber and gun vacuum of 1.3×10^{-5} and 1×10^{-9} mbar respectively. Samples were mounted onto aluminum SEM pin stubs (12 mm diameter, Agar Scientific, Essex, UK) and sputtered with a thin layer of Au/Pd (8 V, 30 s) was sputtered onto the electrodes using an SCP7640 coater (Polaron, Hertfordshire, UK). Thermogravimetric Analysis (TGA) was performed using a Discovery Series SDT 650 controlled by Trios Software (TA Instruments, DA, USA). Samples were mounted in alumina pans (90 µL) and tested using a ramp profile (10 °C min^{-1}) from 0 – 800 °C under N_2 (100 mL min^{-1}). X-ray Photoelectron Spectroscopy (XPS) data were acquired using an AXIS Supra (Kratos, UK), equipped with an Al X-ray source (1486.6 eV) operating at 300 W in order to perform survey scans and 450 W for narrow scans. All X-rays were mono-chromated using a 500 mm Rowland circle quartz crystal X-ray mirror. The angle between X-ray source and analyzer was 54.7° with an electron energy analyzer: 165 mm mean radius hemispherical sector analyzer operating in fixed analyzer transmission mode, pass energy 160 eV for survey scans and 40 eV narrow scans. A detector with delay line detector with a multichannel plate was utilized.

2.5. Electrochemical Activation

The AMEs were treated in 0.5 M NaOH by using Chronoamperometry at +1.4 and −1 V with various time treatments (200 and 1200 s per each step, respectively) in an asymmetric setup. Ni wire and Ag/AgCl were used as counter and reference electrodes, respectively. The solution was purged in N_2 for 10 min before electrochemical treatment.

2.6. Electrochemical Evaluations

To optimize the condition of electrode treatment before use in a full cell supercapacitor, experiments were performed utilizing an asymmetric set-up. For the full cell measurements, a symmetric setup was used. The electrochemical evaluations were carried out in 17 M $NaClO_4$. A length of Ni wire and Ag/AgCl (3 M KCl) were used as counter and reference electrode, respectively. The solution was purged in N_2 for 10 min before the electrochemical test. The areal capacitance obtained from CV (C_{cv}) was found using Equation (1),[23] where $\int IdV$ is the integral area in the discharge region of the CV response, v is the sweep rate (V s^{-1}), ΔV is the window voltage of discharge region (V), A is the geometrical area of the electrode from the CAD file (in cm^2).

$$C_{cv} = \frac{\int IdV/v}{A\Delta V} \tag{1}$$

The areal capacitance obtained from the Galvanostatic charge–discharge technique (C_{CD}) was estimated corresponding to Equation (2), where I is the applied current (in amps), Δt is the time of discharging step (in s), ΔV is the discharging potential window (excluding Ohmic drop).

$$C_{CD} = \frac{I\Delta t}{A\Delta V} \tag{2}$$

The energy (E) and power (P) densities of the SCs were calculated according to Equations (3) and (4), respectively,[23,24]

$$E = \frac{1}{2} C_{CD} (\Delta V)^2 \left(\frac{1}{3600}\right) \tag{3}$$

$$P = \frac{E}{\Delta t}(3600) \tag{4}$$

Electrochemical impedance spectroscopy (EIS) was collected in the frequency range of 0.01 to 100000 Hz at open circuit voltage, with an amplitude of 10 mV. The entire electrochemical tests were measured using Metohm AUTOLAB potentiostat (PGSTAT302N, Eco-Chemie, Utrecht, The Netherlands running NOVA (version 2.1.5)).

The b-value can be calculated from the following equation.[25]

$$i = k\upsilon^b \tag{5}$$

where i is peak current at applied V and υ is scan rate

In case of b values representing the kinetic of charge storage in system, the capacitive-controlled (fast diffusion) and diffusion-controlled (slow diffusion) processes contain the b values of 1 and 0.5, respectively. After taking the log over equation, the b value is obtained in the slope of log current versus the logarithm of scan rate ($\log i = b \log \upsilon + k$).

To find the contribution of the capacitive-controlled (fast diffusion) and diffusion-controlled (slow diffusion) processes, Equation S2 (Supporting Information) can be expressed to the below equation.

$$i = k_1\upsilon^1 + k_2\upsilon^{0.5} \tag{6}$$

where k_1 and k_2 are constants. $k_1\upsilon^1$ and $k_2\upsilon^{0.5}$ are attributed to the current contribution from capacitive-controlled (fast diffusion) and diffusion-controlled (slow diffusion) processes,

respectively. multiplying by $1/v^{0.5}$ on both sides of Equation S3 (Supporting Information) provides,

$$iv^{-0.5} = k_1 v^{0.5} + k_2 \quad (7)$$

The slope and y-intercept of linear plot of $i\ v^{-0.5}$ and $v^{0.5}$ are k_1 and k_2, respectively.

3. Results and Discussion

3.1. Workflow

Figure 1A shows a schematic illustrating each step of processing recycled PLA waste into a high-performance, Additively Manufactured SC. First, recycled PLA, PEG, and conductive CB were melt compounded in a volume ratio of 67.5:10:22.5 using a high-shear mixer. The composite material was cooled and shredded before being melted and extruded into a filament suitable for printing by FFF. This filament was then used to print electrodes as either non-porous, solid electrodes, or porous, mesh-like structures, as shown in Figure 1B. The printed electrodes were activated using chronoamperometry in an alkali solution, as this has been shown to remove surface PLA thereby exposing an increased amount of conductive filler and improving electrode performance.[26] Once activated, the capacitive properties of the electrodes were measured in a 17 M $NaClO_4$ WIS electrolyte either as part of a half-cell alongside standard reference and counter electrodes or as part of a fully 3D printed, full cell consisting of two Additively Manufactured electrodes plus other non-conductive 3D printed components.

3.2. Thermal Characterization of Recycled Filament

After compounding, the thermal properties of the bespoke filament were analyzed by simultaneous TGA/DSC and compared to both the neat, recycled PLA and commercially available CB/PLA. This information is important for several reasons: first, to establish whether the historical thermal processing of the recycled PLA and subsequent processing into a conductive filament affected its thermal stability; second, to determine the effects of PEG on the thermal properties of the polymer composite; and finally, to determine the mass of conductive filler present in each composite filament, which would be expected to directly influence its electrical properties.

TGA data for the recycled PLA, bespoke filament, and commercial CB/PLA are shown in Figure 1C and the onset temperatures (T_o) of degradation, final masses, and non-polymer filler contents for each material are given in **Table 1**. Qualitatively, the presence of CB filler causes a reduction in the rate of thermal decomposition, and CB is presumed to make up most of the final mass of the sample after heating has been completed. However, the initial onset temperature (T_{o1}) for each material is similar, with all T_{o1} being at ≈300–305 °C. This suggests that the presence of CB does not change the chemistry of the decomposition process, but rather the particles act as physical barriers for gas diffusion out of the polymer.[27] Furthermore, the similarity in T_{o1} indicates that the recycling process and further thermal processing have not caused deterioration to the thermal stability of the PLA. The commercial sample also shows a second onset of decomposition (T_{o2}); this is speculated to be a decomposition of the plasticizer listed by the manufacturer to be a component of the material.[28]

Table 1. Compilation of the data obtained through TGA analysis on the recycled PLA feedstock, recycled conductive filament, and commercial CB/PLA filament. Highlighting the degradation onset temperatures, final masses, and filler content levels.

Sample	T_{o1}/°C	T_{o2}/°C	Final mass/wt.%	Filler content/%
Natural PLA	305 ± 5	n/a	3 ± 2	0
Bespoke	301 ± 2	n/a	28.70 ± 0.03	26 ± 2
ProtoP	304 ± 2	436 ± 4	24 ± 2	21 ± 3

The filler contents listed in Table 1 are lower than the final mass for each material as it is necessary to consider charring of the PLA in the nitrogen atmosphere, which means that some residual mass is left in the sample pan even for pure PLA. Filler content is simply taken as the final mass of the composite minus the average charred mass of PLA left in the sample pan. Using this method, the filler content of the commercial filament was found to be (21 ± 3) %, which is consistent with the 21.43% filler content listed by the manufacturer.[28] The filler content of the bespoke filament was found to be higher at (26 ± 2) %.

3.3. Production of the AMEs and optimization of Alkaline Treatment

As outlined in the experimental, the solid electrodes studied in this work were produced using standard CAD software to produce an STL file, which was then sliced into the required GCODE for printing. Production of the Mesh electrodes was performed using FullControl G-Code Designer,[22] an open-source software that allows the user to design free from typical FFF restraints, such as the tool path direction which is commonly automated within the slicing process. In this way, the user can individually define each segment of a 3D printer's tool path, with specific printing parameters, to generate the desired GCODE. The Mesh electrodes were drawn using cartesian coordinates with the first layer alternated between ±10 in the x-axis and ±2 in the y-axis, and the second layer alternated between ±10 in the y-axis and ±2 in the x-axis. Each layer had a height of 0.2 mm and was repeated in the z-axis. This created a base Mesh pattern with a stem, which could then be repeated in the z-axis to create an electrode of 6, 12, and 24 times for the different Mesh sizes. The produced GCODE was then printed on a standard FFF printer. Initial characterization of the electrodes was performed using the 6-layer Mesh electrodes, where the activation was optimized first.

To remove non-conductive PLA from as-printed electrode and expose conductive CB filler, electrochemical activation via chronoamperometry in 0.5 M NaOH was carried out for all electrodes. However, the process was first optimized for a mesh of the bespoke filament. This is because, although such activation has been shown to be effective for commercial

conductive filaments and standard electrode shapes, it was unknown the extent to which it affected the properties of the bespoke filament in a high-surface area porous structure. From our previous work,[26] we used the time activation of 200 s for each applied potential. Herein, the time treatment was varied between 200 and 1200 s to observe the suitable condition for this electrode design. After treatment, the electrochemical performance of the electrodes was demonstrated via cyclic voltammetry (CV) in an asymmetric configuration. CV was performed under the window potential in range of –1 to 1.2 V versus Ag/AgCl at 5–100 mV s^{-1} as shown in Figure S1 (Supporting Information). CV profiles show that a small peak was obtained post-activation (Figure S1D,E, Supporting Information) from the pseudocapacitive current. The a_{real} capacitance of the Mesh-1200s, Mesh 200s, and Mesh-0s is presented in Table S1 (Supporting Information) and was found to be 70.3, 46.2, and 3.2 mF cm^{-2} at a scan rate of 5 mV s^{-1}, highlighting how activation of the electrodes significantly increases the performance. This a_{real} capacitance is a function of the electrode thickness and volumetric capacity.[29] Both the Mesh-200s and Mesh-1200s electrodes exhibited good rate capabilities of ≈84% and ≈60% respectively. A cell with high rate capability is able to generate a considerable amount of power, whilst suffering from little polarization even at high current loads.[30] The lower rate capability of the Mesh-1200s electrode is attributed to the impact of activation on the structural integrity of the electrode, as seen in Figure S1F (Supporting Information). Therefore, the Mesh-200s electrode was chosen for further study due to the improved structural integrity and better rate capability.

3.4. Characterization of Activated Electrodes

The effect of electrochemical activation on the morphology, physical, and chemical properties of the mesh electrodes was studied by characterization of a Mesh-200s sample and comparison with a pristine (i.e., untreated) electrode. SEM images of the Mesh pattern, alongside insets of the surface structure, are presented in **Figure 2**A,B for the pristine and Mesh-200s electrode, respectively. The low magnification images demonstrate that the macroscopic, geometric mesh shape of the electrode was not significantly altered by electrochemical activation. By contrast, the high magnification images suggest that the surface of the electrode has been altered, specifically showing a comparatively rougher surface with exposed particle structures which is consistent with removal of surface polymer by the electrochemical treatment. It should be noted that in some cases the lines printed can be smaller than the nozzle width of 0.4 mm due to natural variation in the filament diameter when loading with high levels of filler.

XPS was performed to investigate the chemical composition of the bespoke electrode before and after activation, and the spectra are shown in Figure 2C–F. For the pristine Mesh electrode, in the C 1s environment specifically (Figure 2C), there is a major peak at a binding energy of 286.0 eV, and three progressively smaller minor peaks at 286.8, 287.8, and 289.1 eV. There is also one especially small peak on the low binding energy shoulder of the major peak, and this has been assigned as sp^2 graphitic carbon, although it could also represent the sp^3 adventitious carbon impurities, which might have slightly higher binding energy. Nonetheless, this peak is used to calibrate the rest of the spectrum by setting its center to 284.3 eV in accordance with graphitic carbon. Ordinarily, the system of four consecutively higher binding energy peaks demonstrated in the C 1s spectrum would be interpreted as four increasingly oxidized carbon environments, for example, in this case, the single environment of PEG plus the three carbon environments of PLA. However, this is not consistent with the corresponding O 1s spectrum, Figure 2E, which shows the same asymmetry toward high binding energies, whereas high binding energy peaks in the C 1s spectrum representing carbon-oxygen bonds should correspond to low binding energy peaks of similar relative intensity in the O 1s spectrum. Instead, it is suggested that the asymmetry in both C 1s and O 1s spectra of the pristine sample are caused by vibrational transitions in PEG alone, which are known to in other polymers to cause asymmetry toward high binding energies.[31] Therefore, it is concluded that XPS of the bespoke filament material shows that it consists mainly of PEG with a small contribution from CB, at least down to the depths resolved by XPS (i.e., a few nm). It is speculated that this PEG-enriched surface is caused by the phase separation of the two polymers during melt processing and subsequent cooling.

By contrast, the surface of the activated bespoke electrode is confirmed with it consisting largely of PLA and CB; fitting this spectrum, Figure 2D requires three peaks of similar intensity which correspond to the three environments in PLA, as well as a larger, lower binding energy peak with asymmetry indicative of graphitic carbon sp^2 environments, plus a small peak at 291.7 eV which is consistent with π–π^* transitions in graphitic material. Similarly, the O 1s spectrum, Figure 2F, of the activated bespoke filament demonstrates two similar intensity peaks which correspond to the main C=O and C—O environments in PLA, plus two small peak shoulders at opposite sides of the main peaks which are consistent with carboxyl groups at PLA chain ends (and possibly increased in concentration by hydrolysis of PLA during activation). XPS, therefore, demonstrates that the bespoke filament has a surface chemistry dominated by PEG and that this surface PEG is removed by activation to expose a surface consisting of a large amount of CB along with PLA.

3.5. Effect of Electrode Design and Material on SC Properties

To determine the role of electrode design, the performance of solid and mesh designs was evaluated. Moreover, the mesh electrode from commercial CB/PLA filament was also studied. The electrochemical storage performance of the supercapacitor can be governed by either diffusion-dominated processes or surface-controlled behavior.[32] Through manipulation of the electrode design from solid electrode to mesh electrode (Figure 1B), the surface area would be enhanced, and also the diffusion to the electrode surface improved. The cyclic voltammetric performance of these variants at different scan rates is presented in Figure S2 (Supporting Information), with a comparison at 50 mV s^{-1} highlighted in **Figure 3**A. This shows that significant improvements in the electrode performance are obtained from both the use of a bespoke filament and through altering

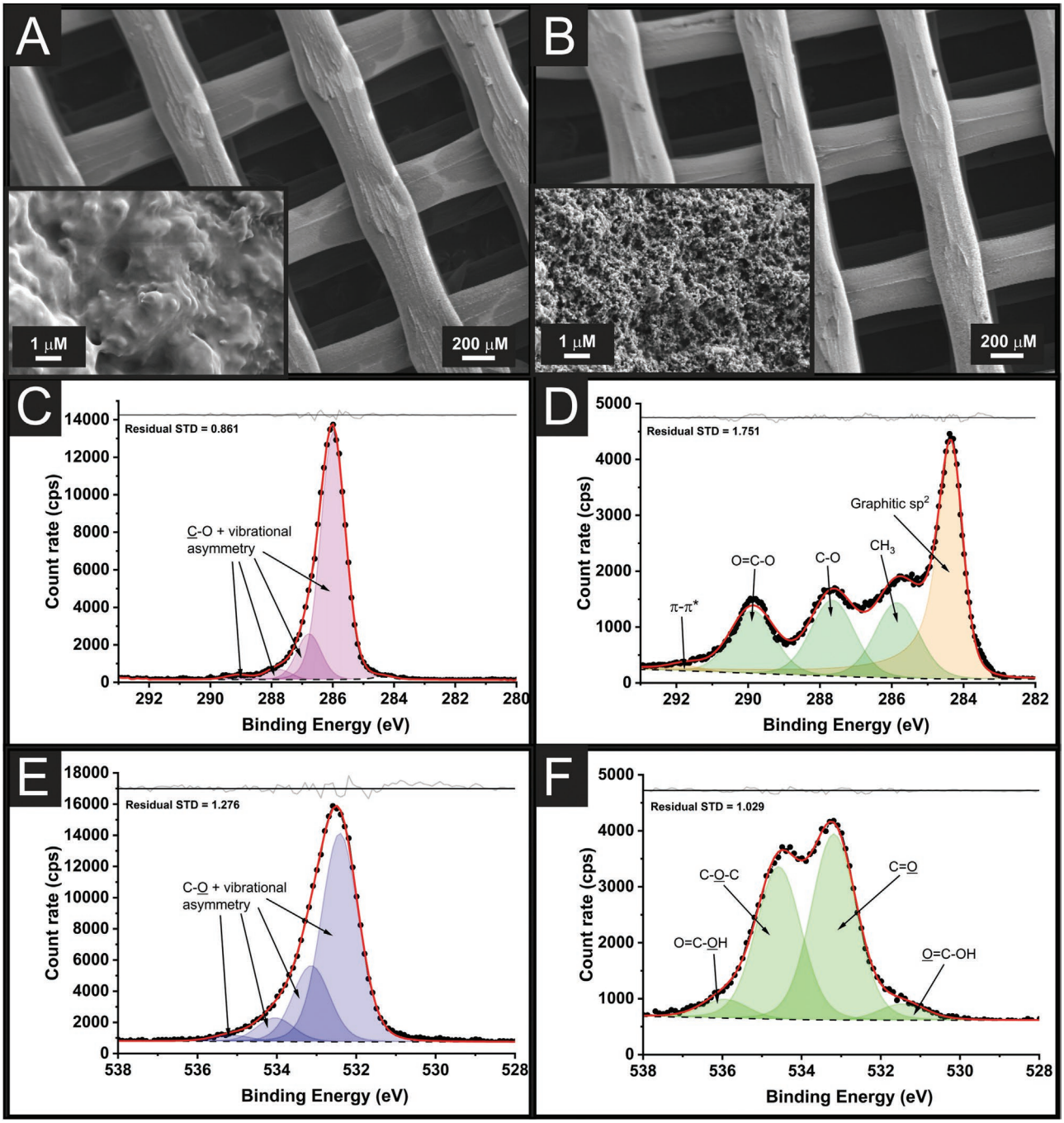

Figure 2. A) SEM image at 50x magnification and (inset) 25000× magnification of the not activated mesh electrode made from recycled conductive PLA. B) SEM image at 50× magnification and (inset) 25000× magnification of the activated mesh-200s electrode made from recycled conductive PLA. C) XPS C1s spectrum for the not activated mesh electrode made from recycled conductive PLA. D) XPS C1s spectrum for the activated mesh-200s electrode made from recycled conductive PLA. E) XPS O1s spectrum for the not activated mesh electrode made from recycled conductive PLA. F) XPS O1s spectrum for the activated mesh-200s electrode made from recycled conductive PLA.

the electrode design. The a_{real} capacitance from CV demonstrated that the mesh electrode from commercial CB/PLA has very poor charge storage, while the electrode from recycled filament provided a capacitance of 37–74 times of the commercial one at 5 mV s^{-1}. Moreover, the mesh electrode obtained not only a higher capacitance but also a better rate capability, Figure 3B, as compared with the solid electrode. In the detail, the mesh electrode achieved double the capacitance and rate capability (at 100 mV s^{-1}) compared with the solid electrode design. This indicated that the mesh design of electrodes can enhance the overall performance of the supercapacitor. To further understand, the Electrochemically Active Surface Area

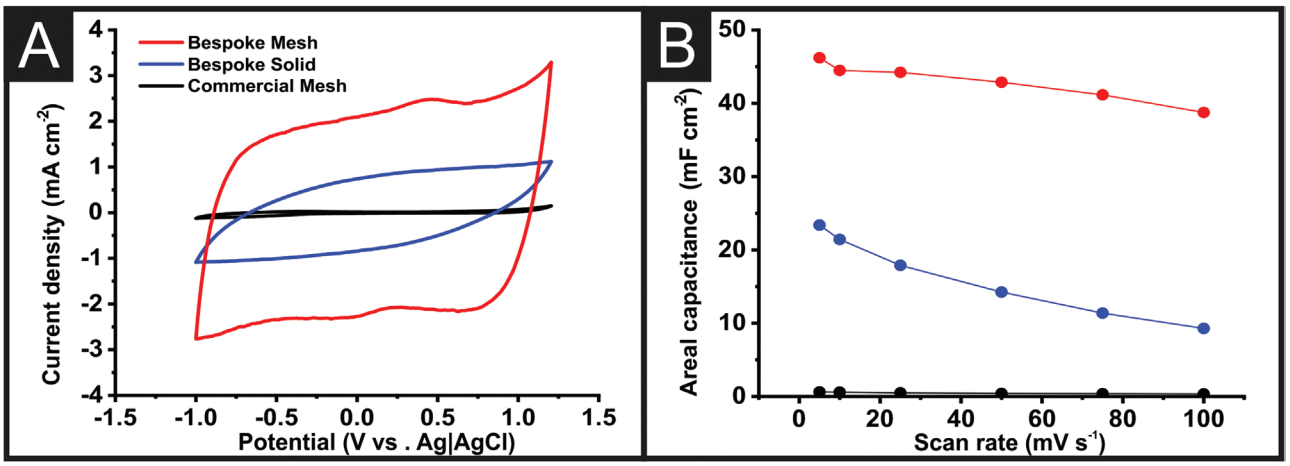

Figure 3. A) Cyclic voltammograms and B) Rate capability comparisons of the asymmetric half cells using mesh AMEs from commercial filament (black) and bespoke recycled filament (red), and solid electrodes from bespoke recycled filament (blue).

(ECSA) of the electrode was determined by using Cdl in the narrow window potential as shown in Figure S3 and Table S3 (Supporting Information). The results exhibited that the mesh electrode provided 3.5 times of ECSA as compared with the solid one (900 and 256 cm^2 for Mesh and Solid, respectively), whilst reducing the amount of filament used by 13.7 ± 0.2%. Thus, by changing the electrode design, a reduction in material and 3.5 times the ECSA can be achieved whilst resulting in improving the overall performance of the supercapacitor. This indicated how changing the electrode design simply using AM can greatly increase the ECSA available, to further investigate the effect of this change, the electrochemical storage mechanism was explored.

3.6. Full Cell Investigation

The symmetrical supercapacitor was assembled from all printed components to demonstrate the cell fabrication via an additive manufacturing process (1 mm of distance between the two electrodes, 900 µL fill volume of electrolyte). The solid design was also fabricated to be a control experiment for investigating the effect of electrode design. The supercapacitor showed 2.2 V of cell voltage. Both the solid and mesh electrode supercapacitor provided pseudo-rectangular shape cyclic voltammograms and isosceles triangle charge-discharge curves, representing the pseudo-capacitance in this cell, **Figure 4**A, Figure S4A,B (Supporting Information). The performances of supercapacitors are presented in Figure 4, Figure S4, and Table S4 (Supporting Information). The results indicated that the performance and rate capability of a mesh-supercapacitor (7.82 mF cm^{-2} at 0.1 mA and 75% at 2.5 mA cm^{-2}) were significantly higher than a solid-supercapacitor (5.28 mF cm^{-2} at 0.1 mA and 42% at 2.5 mA cm^{-2}), correlating to the performance measured using the half-cell configuration. This improvement in performance is attributed to the larger ECSA of the mesh electrodes. This confirmed that the highly porous structure of the mesh-supercapacitor allowed for increased ion accessibility compared to the solid electrode design. Moreover, a high a_{real} capacitance of 7.82 mF cm^{-2} was obtained using a mesh-supercapacitor leading to the highest power and energy densities of 406.43 µW cm^{-2} and 4.82 µWh cm^{-2}, respectively, Figure 4C. Furthermore, the long cycling stability of the AM supercapacitor was determined through Galvanic Charge–Discharge (GCD) at a current density of 1 mA cm^{-2} for 5000 cycles, Figure 4D. The mesh-supercapacitor obtained excellent capacitance retention of 92.86% with 98.48% coulombic efficiency, while the solid full cell provided only 76.89% and 88.24% of capacitance retention and coulombic efficiency, respectively.

To further study the reason behind the high performance of the mesh-supercapacitor, kinetic analysis including CV and Electrochemical Impedance Spectroscopy (EIS) was performed to calculate the b-value, and percentage of capacitance contribution in both electrodes, **Figure 5**. The *b*-value of a system gives evidence toward the electrochemical process occurring in the system; if the b-value is equal to 0.5, then diffusion dominated intercalation processes are implied, whereas a b-value approaching 1 suggests surface-controlled capacitive behavior.[32,33] To evaluate the b-value, the CV of mesh-supercapacitor and solid-supercapacitor was collected at various scan rates (Figure S5, Supporting Information). The *b*-value revealed information about the kinetics of charge storage in device.[25] The capacitive and diffusion-controlled processes produced *b* values of 1 and 0.5, respectively. Figure S5A,B (Supporting Information) present the graphs used to calculate the b-value of solid and mesh-supercapacitor at 1 V. The results indicated that mesh-supercapacitor provided a *b* value close to 1, an increase compared to the solid-supercapacitor, indicating that the highly porous network of mesh design could encourage fast ion-diffusion to the active surface of the electrode, leading to increased capacitive contribution in the system. The b-value calculated for the mesh-supercapacitor of 0.98, Figure 5B, demonstrates that the electrochemical Na^+ storage process is dominated primarily by surface-controlled capacitive behavior.[10]

The EIS technique revealed information about the ion-diffusion resistances of supercapacitors. The Warburg coefficient (σ) was evaluated from the plot of the real part of the impedance (Z') and the reciprocal of the square root of frequency ($\omega^{0.5}$), as shown in **Figure 6**A. The impedance spectrum consists of semi-circular and linear regions at the high

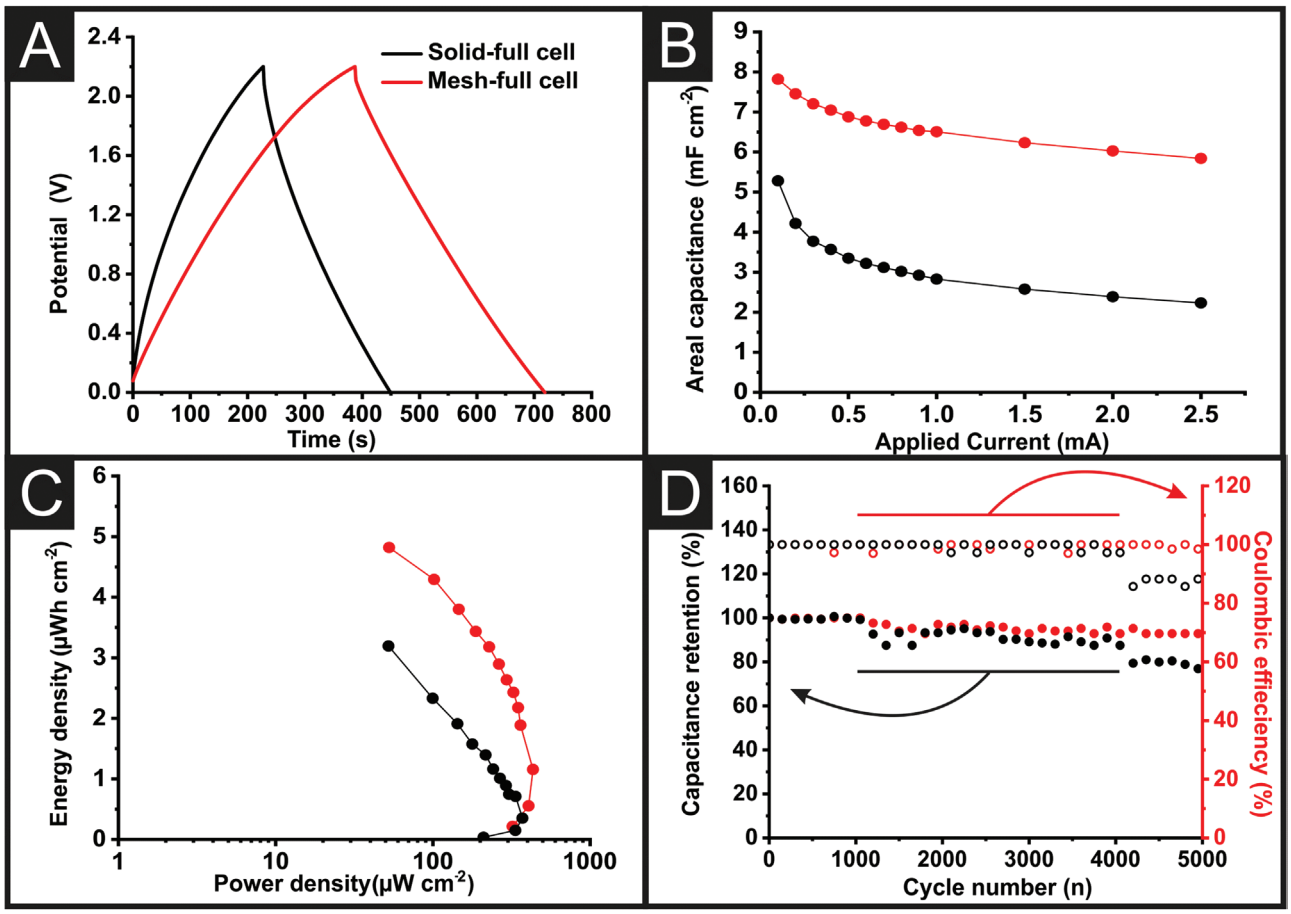

Figure 4. A) GCD responses at 0.1 mA, B) Areal capacitance versus applied current, C) Ragone plot at applied current (0.1 to 2.5 mA), and D) Stability at 2 mA in 17 M $NaClO_4$ of the symmetric full cell supercapacitor using the bespoke recycled filament as a mesh (red) or solid (black) electrode.

and low-frequency regimes, respectively. The X-intercept refers to the equivalent series resistance or internal resistance of the electrode including the resistances of the active material and electrolyte. The semi-circular region is attributed to the charge-transfer resistance (R_{CT}), derived from the charge-transfer process of the electrolyte with the surface of the carbon providing functional groups or dopants. The linear region represents the electrolyte diffusion process, where a steeper slope corresponds to faster ion diffusion.[34] The simplest and most common circuit element for modeling diffusion behavior is the Warburg impedance, which models semi-infinite linear diffusion. From the EIS spectrum, the Warburg coefficient (σ) was determined from a plot of the real part of impedance (Z') as a function of the square root of the frequency. These linear slopes are indicative of the ion diffusion resistance.[35] The mesh-supercapacitor provided a small value of σ (10.34 Ω $s^{-0.5}$), which was significantly lower than the solid-supercapacitor (50.90 Ω $s^{-0.5}$). In addition, Equivalent series resistance (ESR) was also obtained from Nyquist's plot by rough observation. The mesh-supercapacitor had lower ESR than the solid one representing the lower internal resistance in mesh-full cell than mesh (Figure 6B). Both charge transfer resistances (R_{ct}) of the fabricated cells were found to be similar as the same material was used to fabricate each electrode. Thus, the shape of electrode was not changing the properties of material but just encouraging the ion diffusion in the system. The results indicated that the 3D-printed electrode design plays an important role in the production of a high-performance supercapacitor. By designing a mesh electrode with a highly porous structure, the overall performance of supercapacitor was increased due to the larger ECSA and faster kinetic charge storage. This work highlights how high-value products can be produced from recycled post-industrial plastic waste, whilst being further improved through the flexibility of additive manufacturing. Further work in this field can go in various directions from varying the plastics recycled, incorporating other recycled additives, or improving the design of platforms through AM.

4. Conclusions

In this study we present an additively manufactured full cell symmetric supercapacitor produced from recycled post-industrial plastic waste, presenting a paradigm shift in how waste plastic can be utilized to produce high-value products. The additive manufacturing feedstock was produced through the incorporation of carbon black (CB, 22.5 v/v%) as the conductive filler and polyethylene glycol (PEG, 10 v/v%) as a plasticizer into

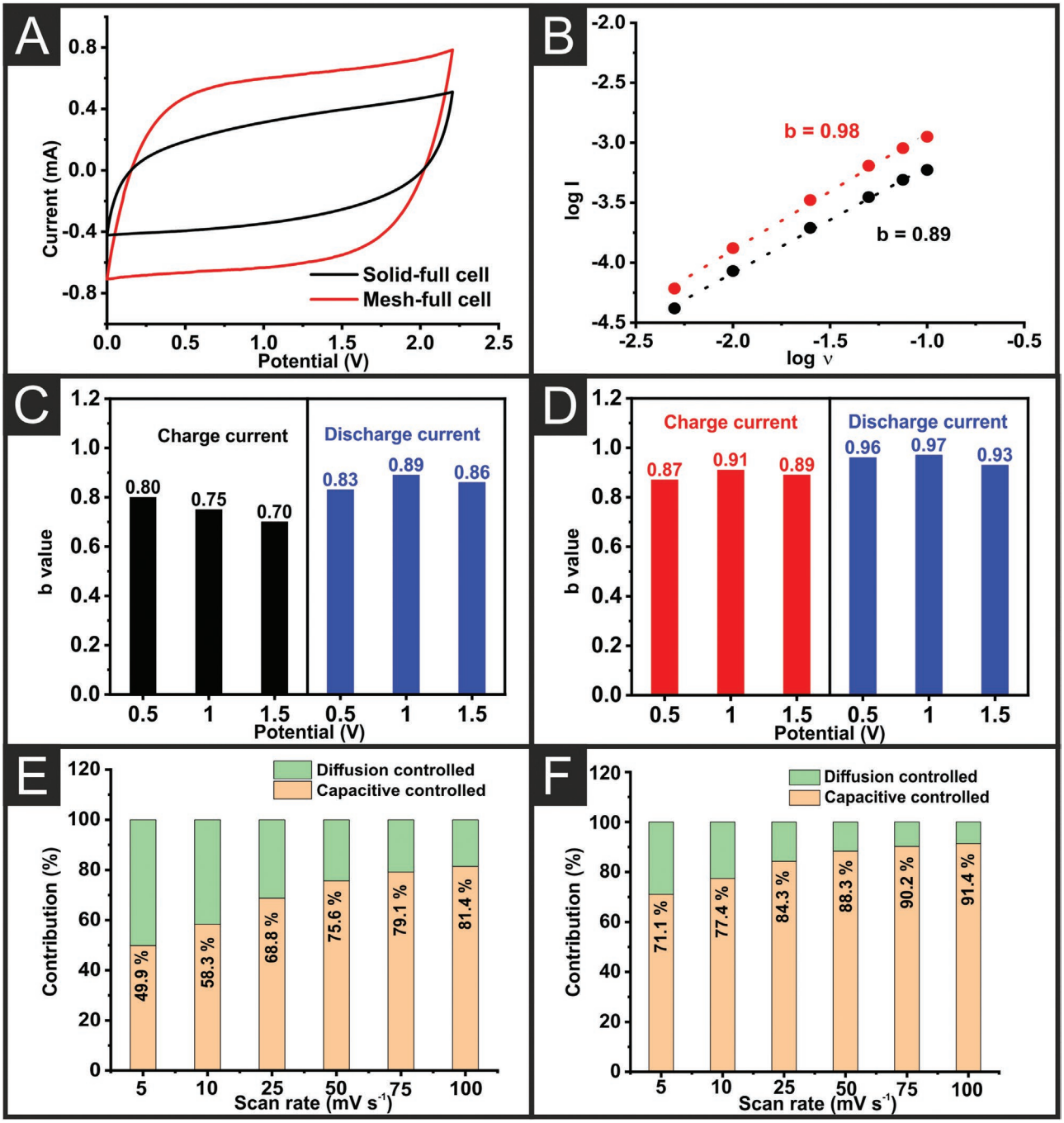

Figure 5. A) CV responses at 50 mV s^{-1} for the symmetric solid-full cell (black) and mesh-full cell (red), B) b value at 1 V of applied voltage, C,D) b value at various applied potentials (Solid and Mesh design respectively), and E,F) Histograms of the capacitance contribution at 1 V with average value from charge and discharge current through the capacitive and diffusion processes in 17 M $NaClO_4$ of symmetric full cell supercapacitor (Solid and Mesh design respectively).

the base polymer or recycled coffee pod poly(lactic acid) (PLA, 67.5 v/v%. It was seen that the recycled bespoke filament was capable of capacitance of over 75 times a commercially available PLA/CB filament in 17 M $NaClO_4$. Additionally, we show how the performance of additively manufactured supercapacitors can be drastically improved through the manipulation of the electrode geometries. Utilizing FullControl software allowed for the generation of a mesh design, which significantly increased the electrochemical surface area of the electrode. This led to a vast improvement in ion adsorption and rapid ion accessibility compared to a solid electrode of the same dimensions, with a 13.7% reduction in material usage and a material cost of £0.15 per electrode. This work demonstrates a paradigm shift in the fabrication of low-cost and high-performance supercapacitors from recycled waste that could be applied in the field of energy storage architectures.

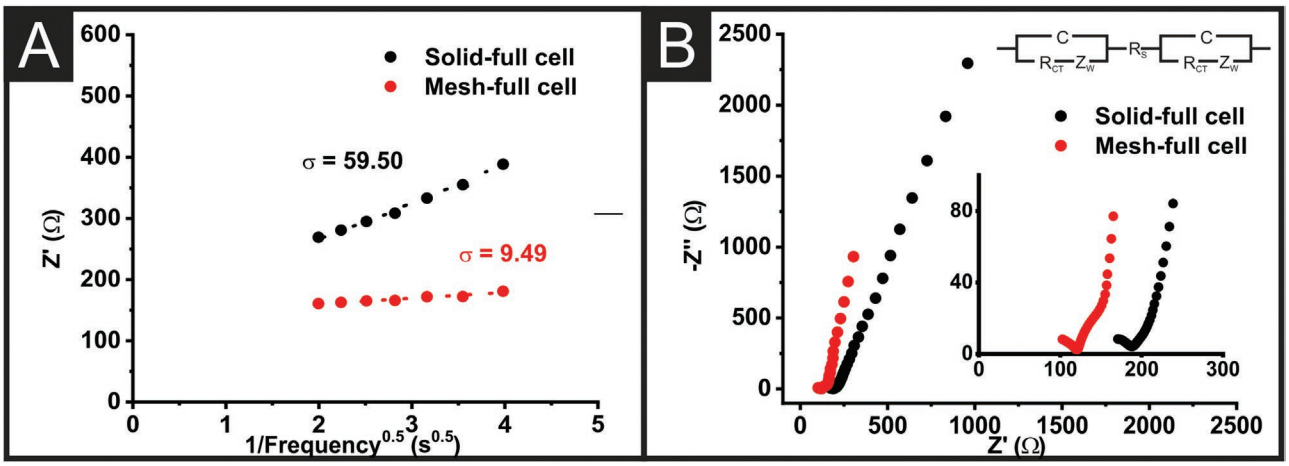

Figure 6. A) *Z′* plotted against the reciprocal of the square root of frequency in the intermediate frequency range of the symmetric Solid (black) and Mesh (red) full cell. B) EIS spectra for the symmetric Solid (black) and Mesh (red) full cell.

Supporting Information

Supporting Information is available from the Wiley Online Library or from the author.

Acknowledgements

This paper was developed as part of the TRANSFORM-CE project, a transnational cooperation project supported by the Interreg North-West Europe program as part of the European Regional Development Fund (ERDF). PW thanks the Vidyasirimedhi Institute of Science and Technology (VISTEC) for financial support.

Conflict of Interest

The authors declare no conflict of interest.

Data Availability Statement

The data that support the findings of this study are available on request from the corresponding author. The data are not publicly available due to privacy or ethical restrictions.

Keywords

3D-printing, Circular Economy, Circular economy electrochemistry, recycled additive manufacturing, recycled conductive poly(lactic acid), supercapacitors

Received: September 22, 2022
Revised: October 20, 2022
Published online:

[1] a) E. Agathokleous, I. Iavicoli, D. Barceló, E. J. Calabrese, *J. Hazard. Mater.* **2021**, *417*, 126035; b) S. S. Ali, T. Elsamahy, E. Koutra, M. Kornaros, M. El-Sheekh, E. A. Abdelkarim, D. Zhu, J. Sun, *Sci. Total Environ.* **2021**, *771*, 144719; c) B. Trotter, A. Ramsperger, P. Raab, J. Haberstroh, C. Laforsch, *Sci. Rep.* **2019**, *9*, 5889.

[2] B. Bridgens, M. Powell, G. Farmer, C. Walsh, E. Reed, M. Royapoor, P. Gosling, J. Hall, O. Heidrich, *J. Cleaner Prod.* **2018**, *189*, 145.

[3] G. C. Nobre, E. Tavares, *J. Cleaner Prod.* **2021**, *314*, 127973.

[4] A. G.-M. Ferrari, N. Hurst, E. Bernalte, R. Crapnell, M. Whittingham, D. Brownson, C. E. Banks, *Analyst* **2022**, *147*, 5121.

[5] M. J. Whittingham, R. D. Crapnell, C. E. Banks, *Anal. Chem.* **2022**, *94*, 13540.

[6] Z. Rymansaib, P. Iravani, E. Emslie, M. Medvidović-Kosanović, M. Sak-Bosnar, R. Verdejo, F. Marken, *Electroanalysis* **2016**, *28*, 1517.

[7] J. G. Escobar, E. Vaněčková, Š. N. Lachmanová, F. Vivaldi, J. Heyda, J. Kubišta, V. Shestivska, P. Španěl, K. Schwarzová-Pecková, J. Rathouský, *Electrochim. Acta* **2020**, *360*, 136984.

[8] K.-E. Guima, V. H. Souza, C. A. Martins, *RSC Adv.* **2019**, *9*, 15158.

[9] E. Vaněčková, M. Bouša, V. Shestivska, J. Kubišta, P. Moreno-García, P. Broekmann, M. Rahaman, M. Zlámal, J. Heyda, M. Bernauer, *ChemElectroChem* **2021**, *8*, 2137.

[10] a) W. Zong, N. Chui, Z. Tian, Y. Li, C. Yang, D. Rao, W. Wang, J. Huang, J. Wang, F. Lai, *Adv. Sci.* **2021**, *8*, 2004142; b) W. Zong, H. Guo, Y. Ouyang, L. Mo, C. Zhou, G. Chao, J. Hofkens, Y. Xu, W. Wang, Y. E. Miao, *Adv. Funct. Mater.* **2022**, *32*, 2110016.

[11] a) M. J. Whittingham, R. D. Crapnell, E. J. Rothwell, N. J. Hurst, C. E. Banks, *Talanta Open* **2021**, *4*, 100051; b) J. Scremin, I. V. J. Dos Santos, J. P. Hughes, A. G.-M. Ferrari, E. Valderrama, W. Zheng, X. Zhong, X. Zhao, E. J. Sartori, R. D. Crapnell, *Nanoscale* **2020**, *12*, 18214.

[12] a) R. D. Crapnell, E. Bernalte, A. G.-M. Ferrari, M. J. Whittingham, R. J. Williams, N. J. Hurst, C. E. Banks, *ACS Meas Sci Au* **2021**, *2*, 167; b) H. M. Elbardisy, E. M. Richter, R. D. Crapnell, M. P. Down, P. G. Gough, T. S. Belal, W. Talaat, H. G. Daabees, C. E. Banks, *Anal. Methods* **2020**, *12*, 2152.

[13] a) A. S. Aricò, P. Bruce, B. Scrosati, J.-M. Tarascon, W. van Schal kwijk, *Nat. Mater.* **2005**, *4*, 366; b) X. Zhang, L. Hou, A. Ciesielski, P. Samorì, *Adv. Energy Mater.* **2016**, *6*, 1600671.

[14] a) Y. Zhu, S. Murali, M. D. Stoller, K. J. Ganesh, W. Cai, P. J. Ferreira, A. Pirkle, R. M. Wallace, K. A. Cychosz, M. Thommes, D. Su, E. A. Stach, R. S. Ruoff, *Science* **2011**, *332*, 1537; b) P. Simon, Y. Gogotsi, *Acc. Chem. Res.* **2013**, *46*, 1094; c) Z. Niu, W. Zhou, J. Chen, G. Feng, H. Li, W. Ma, J. Li, H. Dong, Y. Ren, D. Zhao, S. Xie, *Energy Environ. Sci.* **2011**, *4*, 1440; d) A. Izadi-Najafabadi, S. Yasuda, K. Kobashi, T. Yamada, D. N. Futaba, H. Hatori, M. Yumura, S. Iijima, K. Hata, *Adv. Mater.* **2010**, *22*, E235; e) Z. Yang, J. Tian, Z. Yin, C. Cui, W. Qian, F. Wei, *Carbon* **2019**, *141*, 467.

[15] P. Sharma, T. S. Bhatti, *Energy Convers. Manage.* **2010**, *51*, 2901.

[16] C. Liu, Z. Yu, D. Neff, A. Zhamu, B. Z. Jang, *Nano Lett.* **2010**, *10*, 4863.
[17] M. Inagaki, H. Konno, O. Tanaike, *J. Power Sources* **2010**, *195*, 7880.
[18] C. W. Foster, M. P. Down, Y. Zhang, X. Ji, S. J. Rowley-Neale, G. C. Smith, P. J. Kelly, C. E. Banks, *Sci. Rep.* **2017**, *7*, 42233.
[19] a) J. V. Vaghasiya, C. C. Mayorga-Martinez, M. Pumera, *Adv. Funct. Mater.* **2021**, *31*, 2106990; b) C. W. Foster, H. M. Elbardisy, M. P. Down, E. M. Keefe, G. C. Smith, C. E. Banks, *Chem. Eng. J.* **2020**, *381*, 122343; c) K. Ghosh, S. Ng, C. Iffelsberger, M. Pumera, *Appl. Mater. Today* **2022**, *26*, 101301; d) C. W. Foster, G.-Q. Zou, Y. Jiang, M. P. Down, C. M. Liauw, A. Garcia-Miranda Ferrari, X. Ji, G. C. Smith, P. J. Kelly, C. E. Banks, *Batteries Supercaps* **2019**, *2*, 448.
[20] M. P. Down, E. Martínez-Periñán, C. W. Foster, E. Lorenzo, G. C. Smith, C. E. Banks, *Adv. Energy Mater.* **2019**, *9*, 1803019.
[21] A. García-Miranda Ferrari, J. L. Pimlott, M. P. Down, S. J. Rowley-Neale, C. E. Banks, *Adv. Energy Mater.* **2021**, *11*, 2100433.
[22] A. Gleadall, *Addit. Manuf.* **2021**, *46*, 102109.
[23] S. Kalasina, N. Phattharasupakun, T. Maihom, V. Promarak, T. Sudyoadsuk, J. Limtrakul, M. Sawangphruk, *Sci. Rep.* **2018**, *8*, 12192.
[24] Q. Wang, B. Qin, X. Zhang, X. Xie, L. e. Jin, Q. Cao, *J. Mater. Chem. A* **2018**, *6*, 19653.
[25] a) J. Wang, J. Polleux, J. Lim, B. Dunn, *J. Phys. Chem. C* **2007**, *111*, 14925; b) H.-S. Kim, J. B. Cook, H. Lin, J. S. Ko, S. H. Tolbert, V. Ozolins, B. Dunn, *Nat. Mater.* **2017**, *16*, 454.
[26] E. M. Richter, D. P. Rocha, R. M. Cardoso, E. M. Keefe, C. W. Foster, R. A. A. Munoz, C. E. Banks, *Anal. Chem.* **2019**, *91*, 12844.
[27] J. Guo, C.-H. Tsou, Y. Yu, C.-S. Wu, X. Zhang, Z. Chen, T. Yang, F. Ge, P. Liu, M. R. D. Guzman, *Iranian Polymer Journal* **2021**, *30*, 1251.
[28] Proto-pasta, Safety Data Sheet, https://cdn.shopify.com/s/files/1/0717/9095/files/CDP1xxxx_SDS.pdf?1992606272897634343 (accessed: May 2022).
[29] K. G. Gallagher, S. E. Trask, C. Bauer, T. Woehrle, S. F. Lux, M. Tschech, P. Lamp, B. J. Polzin, S. Ha, B. Long, *J. Electrochem. Soc.* **2015**, *163*, A138.
[30] M. M. Kalantarian, S. Asgari, P. Mustarelli, *J. Mater. Chem. A* **2014**, *2*, 107.
[31] CasaXPS, Asymmetry of Peaks in the XPS of Polymers, http://www.casaxps.com/help_manual/manual_updates/AsymmetryofPeaksintheXPSofPolymers.pdf (accessed: May 2022).
[32] V. Augustyn, J. Come, M. A. Lowe, J. W. Kim, P.-L. Taberna, S. H. Tolbert, H. D. Abruña, P. Simon, B. Dunn, *Nat. Mater.* **2013**, *12*, 518.
[33] J. Qian, F. Wu, Y. Ye, M. Zhang, Y. Huang, Y. Xing, W. Qu, L. Li, R. Chen, *Adv. Energy Mater.* **2018**, *8*, 1703159.
[34] a) N. Ma, N. Phattharasupakun, J. Wutthiprom, C. Tanggarnjanavalukul, P. Wuanprakhon, P. Kidkhunthod, M. Sawangphruk, *Electrochim. Acta* **2018**, *271*, 110; b) N. Phattharasupakun, J. Wutthiprom, S. Kaenket, T. Maihom, J. Limtrakul, M. Probst, S. S. Nagarkar, S. Horike, M. Sawangphruk, *Chem. Commun.* **2017**, *53*, 11786.
[35] a) N. O. Laschuk, E. B. Easton, O. V. Zenkina, *RSC Adv.* **2021**, *11*, 27925; b) T. Liu, Z. Zhou, Y. Guo, D. Guo, G. Liu, *Nat. Commun.* **2019**, *10*, 1179; c) S. Tagliaferri, G. Nagaraju, A. Panagiotopoulos, M. Och, G. Cheng, F. Iacoviello, C. Mattevi, *ACS Nano* **2021**, *15*, 15342; d) X. L. Wu, Y. G. Guo, J. Su, J. W. Xiong, Y. L. Zhang, L. J. Wan, *Adv. Energy Mater.* **2013**, *3*, 1155; e) B. Yao, S. Chandrasekaran, H. Zhang, A. Ma, J. Kang, L. Zhang, X. Lu, F. Qian, C. Zhu, E. B. Duoss, *Adv. Mater.* **2020**, *32*, 1906652.
[36] a) B. Yao, H. Peng, H. Zhang, J. Kang, C. Zhu, G. Delgado, D. Byrne, S. Faulkner, M. Freyman, X. Lu, M. A. Worsley, J. Q. Lu, Y. Li, *Nano Lett.* **2021**, *21*, 3731; b) B. Yao, S. Chandrasekaran, J. Zhang, W. Xiao, F. Qian, C. Zhu, E. B. Duoss, C. M. Spadaccini, M. A. Worsley, Y. Li, *Joule* **2019**, *3*, 459.